Emerging modes of collective cell migration induced by geometrical constraints

Sri Ram Krishna Vedula[a,1], Man Chun Leong[b,1], Tan Lei Lai[c], Pascal Hersen[a,d], Alexandre J. Kabla[e], Chwee Teck Lim[a,b,f,g,2], and Benoît Ladoux[a,d,2]

[a]Mechanobiology Institute, National University of Singapore, Singapore 117411; [b]National University of Singapore Graduate School for Integrative Sciences and Engineering, National University of Singapore, Singapore 117576; [c]Institute of High Performance Computing, Agency for Science, Technology, and Research, Singapore 138632; [d]Laboratoire Matière et Systèmes Complexes (MSC), Centre National de la Recherche Scientifique Unité Mixte de Recherche 7057, Université Paris Diderot, F-75205 Paris cedex 13, France; [e]Engineering Department, University of Cambridge, Cambridge CB2 1PZ, United Kingdom; and [f]Division of Bioengineering and [g]Department of Mechanical Engineering, National University of Singapore, Singapore 117576

Edited by David A. Weitz, Harvard University, Cambridge, MA, and approved June 25, 2012 (received for review November 28, 2011)

The role of geometrical confinement on collective cell migration has been recognized but has not been elucidated yet. Here, we show that the geometrical properties of the environment regulate the formation of collective cell migration patterns through cell–cell interactions. Using microfabrication techniques to allow epithelial cell sheets to migrate into strips whose width was varied from one up to several cell diameters, we identified the modes of collective migration in response to geometrical constraints. We observed that a decrease in the width of the strips is accompanied by an overall increase in the speed of the migrating cell sheet. Moreover, large-scale vortices over tens of cell lengths appeared in the wide strips whereas a contraction-elongation type of motion is observed in the narrow strips. Velocity fields and traction force signatures within the cellular population revealed migration modes with alternative pulling and/or pushing mechanisms that depend on extrinsic constraints. Force transmission through intercellular contacts plays a key role in this process because the disruption of cell–cell junctions abolishes directed collective migration and passive cell–cell adhesions tend to move the cells uniformly together independent of the geometry. Altogether, these findings not only demonstrate the existence of patterns of collective cell migration depending on external constraints but also provide a mechanical explanation for how large-scale interactions through cell–cell junctions can feed back to regulate the organization of migrating tissues.

cell traction forces | collective dynamics | madin darby canine kidney epithelial cells | particle image velocimetry

Collective behavior is a fundamental phenomenon exhibited by a wide variety of systems such as flows in granular matter (1), collective movements of animals (2), self-organization of bacteria (3), and morphogenesis of biological tissues (4). Although collective behaviors have been observed across diverse physical and biological systems, it is increasingly clear that there are broad unifying and common parameters that govern the emergence of this phenomenon such as the density of the constituent particles, the boundary conditions within which the movements occur, and the nature of coupling between the individual particles. In this context, collective behavior in migrating cells is of particular interest as a highly out-of-equilibrium process where cells passively interact with each other and exert active forces in response to their mechanical environment (4). Such collective behavior drives many biological processes such as embryonic development (5), tissue morphogenesis (6), wound healing (7), and tumor metastasis (8, 9). Although single cell dynamics has been extensively studied (10–12), the movement of multicellular structures could not be simply explained by cell autonomous behaviors (13–16). Instead, intercellular interactions and large-scale propagation of mechanical signals (over several cell sizes) are necessary to understand the emergence of mesoscopic behaviors regulating tissue formation and cohesion (6, 17, 18).

Depending on the physiological or pathological conditions under consideration, cells can migrate as large epithelial sheets during wound closure (7), as chains of tumor cells invading the surrounding matrix from the main tumor mass (8), or tubes of neural cells migrating along the lateral line of the zebrafish (19). Whereas studies on single cells suggest that migratory mechanisms are strongly affected by the mechanical constraints of the environment (20), the impact of such constraints on collective migration remains unclear (14, 18). However, both in vivo and in vitro collective migration behaviors occur under a broad range of external constraints that induces diverse morphological behaviors including the appearance of highly motile mesenchymal leader cells (18, 19), the organization of small cohorts of follower cells locally guided by leader cells (21), cryptic lamellipodia formation by cells several rows behind the leading front (7), and the observation of large-scale movements within cell monolayers (17, 22). Moreover, much conflicting evidence has emerged regarding the mechanical regulation of collective cell movements: in vitro traction force mapping shows that an expanding epithelial cell sheet is under a global tensile state (13), whereas recent studies on three-dimensional cell migration in tracks (23) as well as in vivo studies (24) suggest that pushing forces driven by cell-derived compression and cell proliferation could explain further cell expansion and formation of multicellular assemblies. These studies lead to important questions such as the role of the leading front in the guidance of cells behind (18, 25, 26), the influence of internal dynamics on the emergence of collective motions (16, 17), and consequently the physical mechanisms that drive collective migration under various constraints. These intriguing questions are currently debated. Understanding how external constraints influence collective cell behavior might explain some of the observed discrepancies in a large variety of biological processes.

Here, we have developed an original in vitro assay based on microfabrication techniques to determine how collective cell migration responds to well-defined geometric constraints. We show that such constraints can trigger different modes of epithelial cell migration by altering intercellular coordination within the monolayer. Mapping of the velocity field and force distribution reveals that large-scale interactions over distances spanning many cell bodies can be tuned by changing the external confinement as well as the internal dynamics of cell–cell junctions. These experimental findings supported by numerical simulations demonstrate that

Author contributions: S.R.K.V., C.T.L., and B.L. designed research; S.R.K.V., M.C.L., T.L., A.J.K., and B.L. performed research; S.R.K.V., M.C.L., T.L., A.J.K., and B.L. contributed new reagents/analytic tools; S.R.K.V., M.C.L., T.L., P.H., A.J.K., C.T.L., and B.L. analyzed data; and S.R.K.V., M.C.L., C.T.L., and B.L. wrote the paper.

The authors declare no conflict of interest.

This article is a PNAS Direct Submission.

Freely available online through the PNAS open access option.

[1]S.R.K.V. and M.C.L. contributed equally to this work.

[2]To whom correspondence may be addressed. E-mail: ctlim@nus.edu.sg or benoit.ladoux@univ-paris-diderot.fr.

This article contains supporting information online at www.pnas.org/lookup/suppl/doi:10.1073/pnas.1119313109/-/DCSupplemental.

the integrated information within epithelial cell sheets, which leads to collective dynamics, is governed by interplay between external physical cues and cell–cell interactions. This study provides a framework from which the impact of external constraints on collective cell migration can be taken into account for both in vitro and in vivo studies.

Results and Discussion

Migration-Based Assay of Epithelial Cell Sheets Under Geometrical Constraints. We used a combination of various experimental techniques including microcontact printing (27), particle image velocimetry (PIV) (22), and microforce sensor arrays (28) to study the migration of an epithelial cell sheet under geometrical confinement. We designed a fibronectin pattern surrounded by nonadhesive areas (27) that includes a large rectangular reservoir connected to strips of different widths ranging from ≈20 to 400 μm (*Materials and Methods* and Fig. 1*A*). A confluent monolayer was grown inside the reservoir adjacent to a slab of polydimethylsiloxane (PDMS). By doing so (29), we not only ensured that the monolayer was not damaged but we also allowed the cell sheet to migrate upon removal of the slab into the different strips. Providing a free virgin surface by removing the block of PDMS was sufficient to trigger the migration of Madin-Darby canine kidney (MDCK) epithelial cell sheet from the reservoir into the fibronectin strips. Using this assay, collective cell migration was strictly confined into the fibronectin patterns (Fig. 1*B*, Movie S1). After allowing the cell sheet to migrate for at least 4 h, we analyzed simultaneously cell movements within the different channels.

We first studied how the geometrical constraints influence the overall migration velocity of cell sheets. First, we computed the displacement of the leading edge of the monolayer (averaged over several points on the leading cell front between successive images) over the whole observation period and then the average velocity as a function of the width. We observed a linear progression of the leading front independently of the width of the strip (Fig. 1*C*, Fig. S1*A*). However, we observed that the average velocity of the cell front varied with the width of the strips increasing from 22.4 ± 2.2 μm/h for the wider ones (400 μm) to 39 ± 3.9 μm/h for the narrow ones (20 μm) (Fig. 1*D*). Moreover, even if a linear progression of the cell front was observed for all the channels, larger fluctuations were obtained in the narrow strips (20 μm) than in the wider ones (from 100 to 400 μm) (as shown by the standard deviations of the displacement as a function of the width, Fig. 1*C*). In fact, a closer look into the cell sheet migration using our assay shed light on the emergence of different modes of collective cell migration. Cells in the narrow strips (20 μm) showed a contraction-relaxation or caterpillar-like mechanism to move forward (Movie S2), whereas those in the wide strips (400 μm) exhibited a continuous progression. We then sought to determine whether geometrical constraints could alter the shape and density of cells within the cell sheet because both these parameters could affect the migration characteristics of cell populations (30, 31). Accordingly, elongation and orientation index of cells was calculated, distribution of actin stress fibers was visualized, and cell density as a function of the distance away from the leading front was computed. Cells were found to be much more elongated and oriented along the length of the strip in the narrow (20 μm) strips whereas they had no preferred orientation in the wide and intermediate width (400 and 100 μm) strips. Furthermore, some cells at the leading front on the wider strips occasionally developed large lamellipodia and assumed a mesenchymal phenotype reminiscent of leader cells described in previous studies (21). The elongation factor was found to be 1.82 ± 0.05 on the 400 μm and 1.91 ± 0.03 on 100 μm wide strips and increased to 2.52 ± 0.16 in the 20 μm wide strips (Fig. 2*A*). Actin stress fibers were also found to be randomly distributed in the 400 and 100 μm wide strips but directed along the long axis of the strip in the 20 μm wide strips (Fig. 2*B*). Furthermore, on the 400 and 100 μm wide strips, cell density increased from approximately 1 cell/1,000 μm^2 at the leading front to approximately 4 cells/1,000 μm^2 about 600 μm away from the

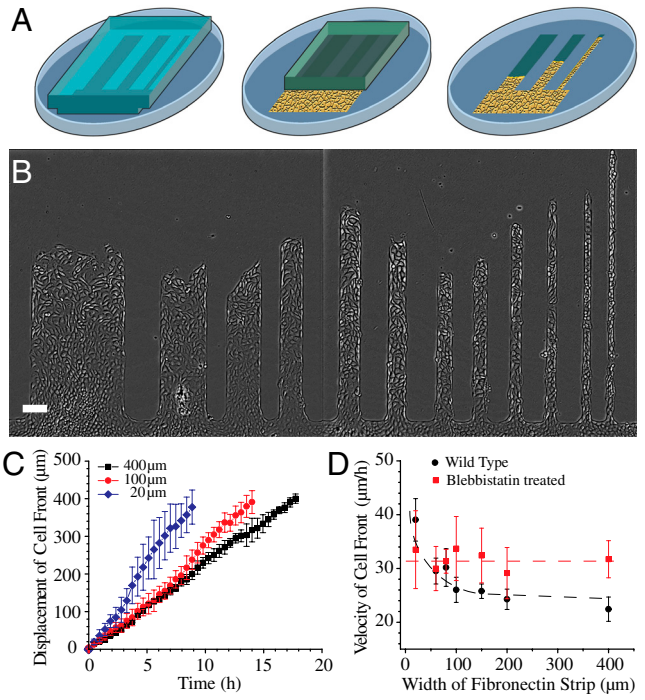

Fig. 1. Migration of MDCK cell sheet on fibronectin strips of different widths. (*A*) Schematic of the fibronectin stamped pattern with a block of PDMS (gray). Cells reach confluence in the reservoir (shown as a yellow area) and migrate into the strips when the PDMS block is lifted (as illustrated by the last step). (*B*) MDCK cell sheets migrating on fibronectin strips of different widths. (*C*) Average displacement of cell front over time in 400, 100, and 20-μm wide strips. (*D*) Velocity of cell front on strips of different widths for untreated (black) and blebbistatin-treated (red) MDCK cells. Dashed lines are a smooth fit to guide the eye. (Scale bar, 100 μm).

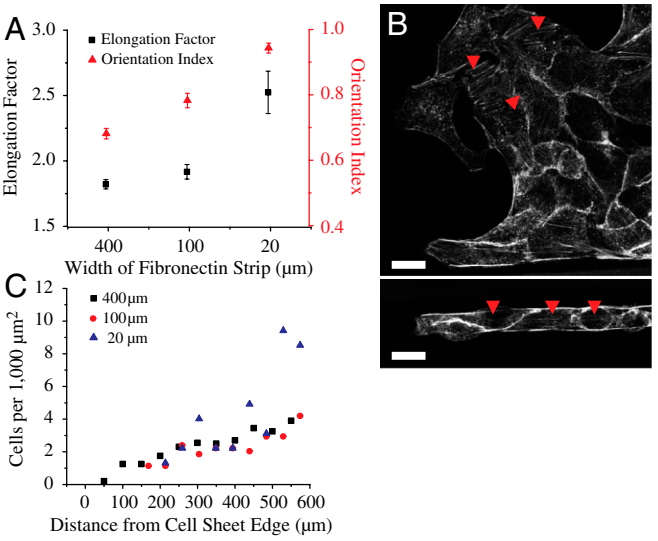

Fig. 2. Width of the fibronectin strip affects the morphology and cell density in the migrating epithelium. (*A*) Elongation factor and orientation index in strips of different widths. (*B*) Actin staining showing random stress fiber distribution in the 400-μm wide (arrow heads,*Upper*) and aligned stress fibers in the 20-μm wide strips (arrow heads,*Lower*). (*C*) Cell density at different distances from the leading front on strips of different widths. (Scale bars, 20 μm).

leading front. On the 20 μm wide strips, cell density showed large sawtooth fluctuations and varied from approximately 1 cell/1,000 μm^2 at the leading front to approximately 9 cells/1,000 μm^2 600 μm away from the leading front (Fig. 2*C*).

Influence of Geometrical Constraints on the Velocity Fields of Migrating Epithelial Cell Sheets. We then asked whether the different migration modes (contraction-relaxation in narrow strips vs. smooth migration in wider strips) induced by geometric confinement arose from the differences in local velocity fields within the epithelial cell sheets revealing correlation length changes of cell movements. To address these questions, we utilized PIV. In the 400 and 100 μm wide strips, velocity vectors of high magnitude (hot or red regions, approximately 35–40 μm/h) were predominantly localized to several rows of cells (approximately 100–150 μm) at the leading front whereas low velocity vectors (cold or blue regions, approximately 15 μm/h) were observed farther away from the leading front (Fig. 3*A*, *Left* and Movie S3). Spatiotemporal analysis of kymographs color coded for velocities also showed that clusters of high velocity vectors were not static but localized to different regions of the cell front at different time points (Fig. 3 *B* and *D*). This result suggests that in the wider strips, several rows of highly motile cells at the leading front pull the slow moving cell sheet behind resulting in significant tension within the sheet (because the cell sheet remains intact). In contrast, in the 20 μm wide strip, PIV analysis showed that large velocities originated anywhere across the whole length of the cell chain and not necessarily close to the leading front (Fig. 3*A*, *Left* and Movie S2). Furthermore, significant negative velocities (opposite to the movement of the overall cell front) were also observed (Fig. 3 *C* and *E*). Such a velocity profile suggests a well-coordinated push-pull mechanism within the cell chain in the narrow strips and correlates well with the contraction and relaxation or caterpillar-like mode of migration observed in phase

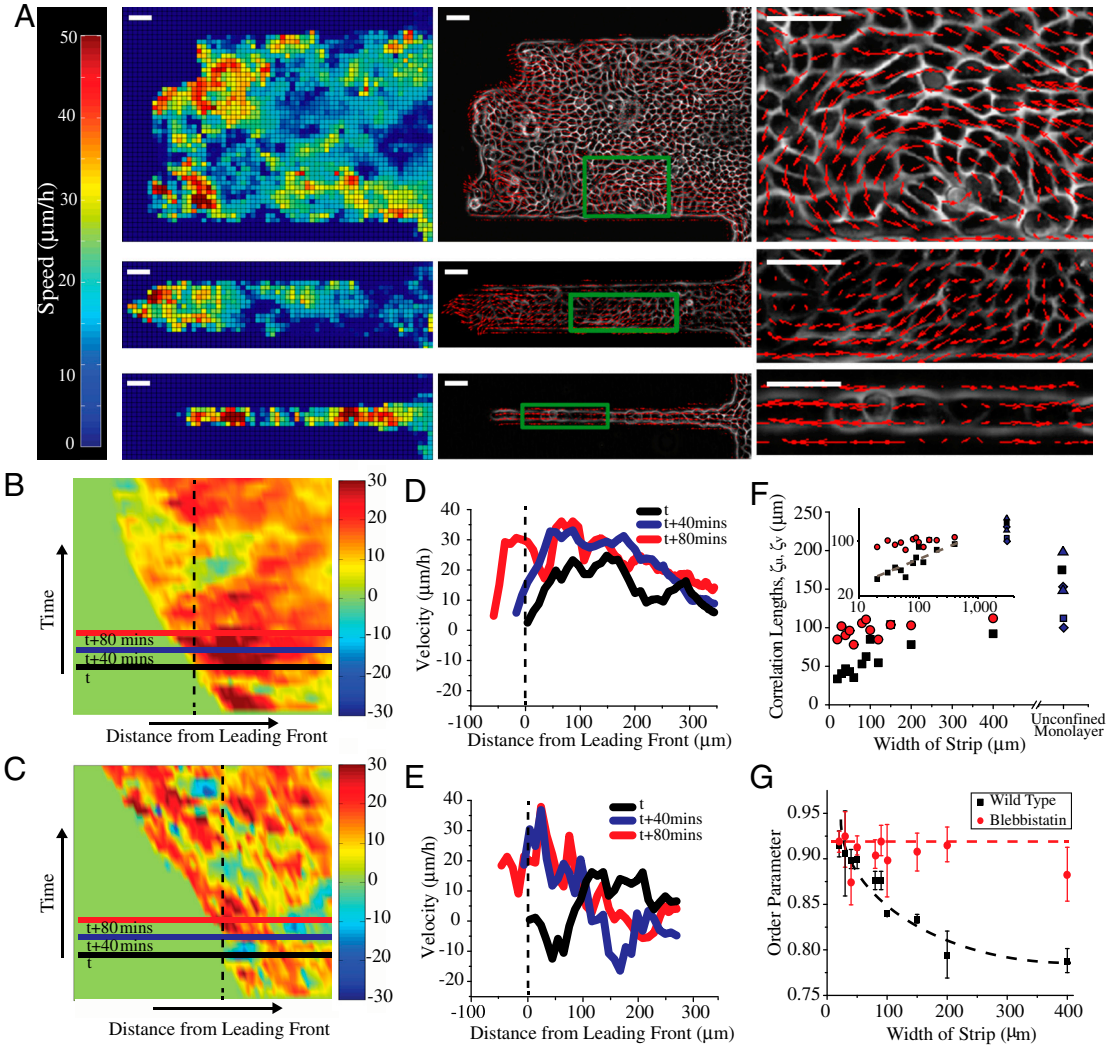

Fig. 3. PIV analysis of migrating epithelial sheets on wide, intermediate, and narrow fibronectin strips. (*A*) Heat map showing spatial distribution of velocity fields at a given instant (*Left*) along 400-μm wide (*Top*), 100-μm wide (*Middle*), and 20-μm wide strips (*Bottom*). Direction of velocity fields (*Center*) showing vortex formation in 400-μm wide strips (*Top*) but not in strips ≤100-μm wide (*Middle* and *Bottom*). Magnified views of region delimited by green boxes. (*Right*) Kymographs of migrating cell sheets color coded for velocities on (*B*) 400-μm and (*C*) 20-μm wide strips. Red color represents large velocity vectors in the direction of the migration of the cell front whereas blue represents velocities directed against the migration of the cell front. Timescale along *y* axis is approximately 10 h. Velocity profile along the lines shown on the kymographs at three different time points on (*D*) 400-μm wide and (*E*) 20-μm wide strips. (*F*) Spatial correlation of velocity vectors perpendicular (ξ_u) and parallel (ξ_v) to the longitudinal axis of the strip. For strips ≤100 μm, ξ_u scales with the width of the strip and saturates to finite values between approximately 120–200 μm for unconfined monolayers (▲, ◆, ■, represent data from refs. 22, 32, and 33, respectively). (*Inset*) Log–log plot of correlation distance as a function of the width of the strips. On the other hand, ξ_v shows a roughly constant value of approximately 100 μm for strips of all widths (red line). (*G*) Order parameter of the velocity vectors in untreated and blebbistatin-treated MDCK cells. Dashed lines highlight the trend of how the order parameter varies with the width of the strip. (Scale bars, 50 μm).

contrast images (Movie S2). A closer analysis of the migration revealed that the contraction-relaxation cycle in the narrow strips spans ≈100 μm (≈3–6 cells, Fig. S1*B*). Such alternating phases of acceleration and stalling appear to be reminiscent of the extension of finger-like shapes in migrating epithelia as previously described (26). However, this observation suggests that although the leading front is important in driving migration of cells into the strips, cell–cell interactions far away from the leading edge also actively contribute to the net progression of the cell monolayer. Interestingly, the magnitudes as well as fluctuations in velocities were higher on the edges of the wider strips rather than in the middle of the strip (Fig. S1*C*). Because cells in this region are confined only on one side, they experience an intermediate behavior between cells in the middle of the wide strip and those in the narrow strips. To further delineate the role of large-scale coordinated movements and correlation length of such movements in regulating the migration modes, we analyzed the direction of the velocity vectors. Large and transient vortices of ≈100 μm in diameter (approximately 10 cells) were observed in the 400 μm wide strips but not in strips of widths ≤100 μm (Fig. 3*A*, *Middle* and *Right* and Movies S4 and S5) in agreement with previous studies based on traditional wound healing assays (30). Consequently, we measured the spatial velocity correlation along the length (ξ_v) and width of the channel (ξ_u), which quantified the distances over which the movements were collectively driven within the monolayer. Previous studies on epithelial cells have shown that large unconfined migrating monolayers led to similar finite values of the correlation lengths within a range comprised between 120 to 200 μm (Fig. 3*F*) (30, 32, 33). Here, the correlation length ξ_u scales with the width of the strips for strips whose width was ≤100 μm. However, in strips >100 μm wide, ξ_u saturates quickly reaching a value of approximately 100 μm, reflecting mostly the internal dynamics of the monolayer (Fig. 3*F*). Interestingly, a similar relationship has been previously described for other physical systems such as sedimenting colloids (34). The velocity fluctuations in colloidal sedimentation varied with the width of the confinement only for dimensions smaller than the characteristic swirl size. By plotting the average velocity fluctuations (perpendicular to the length of the strip) as a function of the width of the fibronectin strips (Fig. S1*E*), we found that these fluctuations scaled with the width of the strip in a fashion similar to that observed for the correlation length. In the parallel direction of the strip, the correlation length, ξ_v, shows a nearly constant value (approximately 100 μm) as a function of the width (Fig. 3*F*). Consequently, it appears that geometrical constraints are sufficient to modulate the dynamics of cell–cell interactions and induce large-scale alignment of cells. To confirm that the geometrical constraints govern a transition in the polarized migration of the multicellular assemblies, we computed the order parameter (*SI Materials and Methods* and Fig. 3*G*) of the velocity vectors. The quantification of this parameter exhibits a significant decrease from 0.92 to 0.79 when increasing the width of the channel from 20 to 400 μm, respectively. These observations are well-supported by recent numerical results showing that the length scale of geometrical constraints could have a strong influence on the emerging directionality in cell populations, irrespective of the dynamics of a leading edge and of potential proliferation effects (35). Considering a population of $N \times N$ motile cells confined in a biperiodic domain, the model exhibits a transition from sheet migration (full alignment) to swirls (no overall alignment) as the size N of the system is increased from a few cells to tens of cells. Consistently with the experiment, the alignment transition is found to occur when N is of the order of the correlation length of the unconstrained case (*SI Materials and Methods* and Fig. S1*D*). This similarity suggests that such a transition is a physical process driven by the internal dynamics of the cell sheet although the overall directionality and caterpillar-like dynamics are still governed by the leading front as described by other models (26). In particular, the order parameter in the experimental system tends to a finite value at large channel widths, consistent with wound healing assays, rather than zero as expected in the simulation. Together, these observations establish that physical constraints affect cell–cell rearrangements and thus the active forces exerted through cell–cell junctions.

Role of Cell–Cell Junctions in Epithelial Cell Migration. Because cell–cell interactions appeared to play a key role in the observed modes of migration, we examined the role of intercellular adhesion proteins. Cell–cell junction proteins such as E-cadherins and their linkage to actin cytoskeleton through various cytoplasmic adaptor molecules (e.g., α-catenin) are crucial to maintain the cohesiveness and physical integrity of epithelial cell sheets (36). Immunostaining for E-cadherin revealed that intercellular contacts were intact in strips of all widths (*SI Materials and Methods* and Fig. S2). To assess further the importance of cell–cell adhesion for coordinated collective migration, we analyzed the migration of MDCK cells in which α-catenin has been stably knocked down and hence cannot form stable intercellular contacts (36). These cells migrated in a highly uncoordinated and random fashion leading to significantly lower migration velocity (approximately 13 μm/h across fibronectin strips of all widths) of the overall cell front compared to normal MDCK cells (Movie S6). A similar migratory behavior was also observed in low calcium medium (Movie S7). Together, these results show that intercellular transmission of mechanical signals across many cells is crucial to observe long-range interactions within the monolayer as well as directed and cohesive motions.

Substrate Traction Forces Reveal Different Modes of Migration. We further hypothesized that the emergence of various modes of migration depending on geometrical confinement could appear as distinct signatures in the magnitude, orientation, spatial, and temporal distribution of substrate traction forces exerted by the cell sheet. To explore this hypothesis, cell sheets were allowed to migrate on strips of flexible micropillars with similar dimensions as the ones previously described (28). As shown by SEM pictures (Fig. S3*A*) and immunostaining experiments (Fig. 4*A* and Fig. S3*B*), the cells were nicely confined on the strips, adhered on the top of the micropillars, and were able to deform the pillars (Fig. 4*B*). We then used live-cell video microscopy to obtain quantitative values of the traction forces exerted by the epithelial cells (see *Materials and Methods*). The average traction force, $\langle F \rangle$, registered in the 400 μm wide strips were higher at the leading front (2.27 ± 0.19 nN), decayed rapidly by 50% to 1.14 ± 0.12 nN at approximately 100 μm away from the front (Fig. 4*B*) and were randomly oriented in all directions (Movie S8). We observed larger traction forces at the leading front on the 20 μm wide strips (2.74 ± 0.26 nN). However, whereas $\langle F \rangle$ exhibited a monotonic decay as a function of the distance from the edge in the 400 μm wide strips, $\langle F \rangle$ showed spikes of forces (approximately 2 to 2.5 nN) much further away from the leading front (Fig. 4*B*), which were predominantly directed along the length of the strip (Movie S9). In an attempt to correlate the traction forces to the differences in migratory patterns observed with PIV, we analyzed the stress ($\langle \sigma_{xx} \rangle$) within the cell sheet along the length of the strip in the 400 and 20-μm wide strips (Fig. S3*C*). As previously described by Trepat et al. (13), the stress, $\langle \sigma_{xx}(D) \rangle$, at a given distance D from the leading edge was obtained by summing the traction forces exerted by cells in the x-direction from the leading edge up to the distance D according to mechanical equilibrium. Our results showed that $\langle \sigma_{xx} \rangle$ initially increased sharply for the cell sheet migrating on 400-μm wide strips (Fig. S3*D*). Such a profile of stress distribution indicated that cells several rows behind the leading front also contributed to the migration of the cell sheet in agreement with previous studies (13, 28). Interestingly, $\langle \sigma_{xx} \rangle$ was found to be lower on the 20-μm wide strips

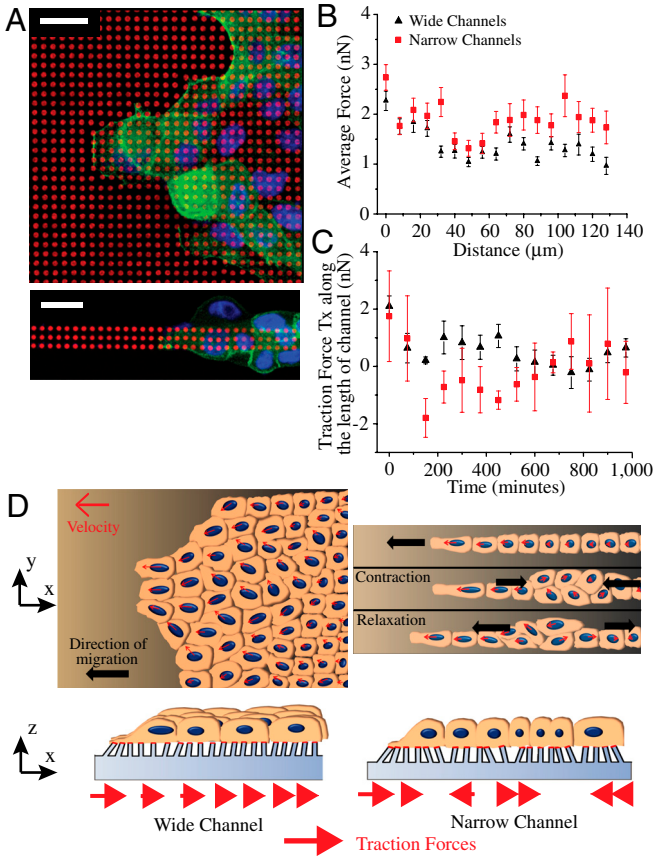

Fig. 4. Geometrical constraints alter spatiotemporal distribution of cell-substrate traction forces. (*A*) MDCK cells migrating on fibronectin (red) stamped micropillar arrays of different widths fixed and stained for actin (green) and nucleus (blue). (*B*) Average cell traction forces as a function of distance from leading front on 400 and 20-μm wide strips. (*C*) Temporal evolution of T_x (component of traction forces along the length of the channel, deflection of pillars opposite the direction of cell sheet migration is considered positive) at a given region in the 400 and 20-μm wide micropillar arrays as the cell sheet migrates over it. The deflections of micropillars in a small window, initially at the cell edge, are tracked over time. (*D*) Cartoon depicting the movement of cells on wide (*Right*) and narrow (*Left*) strips on flat substrates (*Upper*) and micropillar arrays (*Lower*). (Scale bars, 20 μm).

revealing a decrease in the tensile state of the monolayer for about 30–120 μm away from the cell front in highly confined environments (Fig. S3*D*). Moreover, it reached a saturation regime after approximately 100 μm whereas the stress from the wide channel kept on increasing. This result suggested that not only the magnitude of the forces was affected by the physical constraints imposed by the environment but also their directionality because alternative patterns of positive and negative forces could explain such a behavior. We thus analyzed the temporal evolution of the component of traction forces along the length of the channel, T_x, at a defined region in the strip (as the cell sheet or stream moved over it). It showed two distinct differences between the 400 and 20-μm wide strips (Fig. 4*C*). First, the forces decayed rapidly and monotonically with time (2 nN at $t = 0$ to approximately 0.5 nN at $t = 200$ min and small fluctuations of 0.4 nN thereafter) in the 400-μm wide strips whereas spikes of large traction forces (approximately 1 to 2 nN) were observed with the passage of time in the 20-μm wide strips. Secondly, significant negative forces were observed in the 20-μm wide but not in the 400-μm wide strips. Our traction force experiments confirmed that the external constraints induced a switch in epithelial cell migration from a contraction-elongation mechanism to the extension of a cell sheet under a tensile state thereby registering a different traction force pattern (Fig. 4*D*).

Role of Acto-Myosin Contractility in Regulating Different Modes of Migration Induced by Geometrical Constraints. Finally, we hypothesized that the different migration modes could be related to the relative forces that cells exert on their neighbors through acto-myosin-mediated contractility. To modify the dynamical interactions of cell–cell contacts, epithelial cell monolayers were treated with blebbistatin, an inhibitor of myosin II-mediated contractility. We thus studied the migration of cell sheets on strips of different widths in the presence of 50 μM blebbistatin. Morphologically, cells appeared larger and of more uniform density (1 to 2 cells/1,000 μm^2 on 400, 100, and 20-μm wide strips) in the presence of blebbistatin (Fig. S4 and Movie S10). Actin stress fibers were disrupted but the intercellular adhesions (as observed from staining for E-cadherin) remained intact (Fig. S4). Interestingly, we observed that, cells moved in a streamlined and directed fashion independently of the width of the strips (Movie S10). The average velocity of the migrating cell front did not show much variation across strips of different widths (31.7 ± 3.4 μm/h on 400-μm wide strips, 33.6 ± 5.9 μm/h on 100-μm wide strips, and 33.4 ± 7.2 μm/h on the 20-μm wide strips, Fig. 1*D*). PIV analysis showed a more homogenous distribution of velocity fields in both wide and narrow strips than untreated cells (Fig. S5*A*, *Left*). The average velocity fields were also predominantly positive suggesting that most of the individual cells were migrating together along the direction of the migrating cell sheet. Under blebbistatin treatment, the formation of vortices in the wide strips as well as the migration in a caterpillar fashion in the narrow ones disappeared (Fig. S5*A*, *Middle* and *Right* and Movie S10). To further quantify the differences in vortex formation in the blebbistatin-treated and -untreated cells, the order parameter as well as the spatial distribution of angular velocity (rad/h) was calculated from the velocity fields obtained through PIV (Fig. 3*G* and Fig. S5*B*). The order parameter in blebbistatin-treated cells showed a constant value (approximately 0.9) independent of the width of the strip. The curl of the velocity (*SI Materials and Methods*) vectors provided an estimate on the degree of rotational movements. In blebbistatin treated cells, mean angular velocity decreased by approximately 50% from 0.21 rad/h to 0.1 rad/h (Fig. S5*C*, *Top*) and the histogram of angular velocities shifted closer to zero (Fig. S5*C*, *Bottom*). These observations led us to the following prediction: Blebbistatin-treated cells maintained their contact with their neighbors due to strong adhesive steering mechanism (37) but were not able to exert active traction forces through these cell–cell contacts (Fig. S5*D*). Consequently, the length scale that corresponds to long-range cooperative movements under normal conditions appears much larger under the inhibition of myosin II. The internal dynamics within the monolayer that leads to the formation of vortices or a mechanism of contraction-elongation along the cell sheet under various geometrical constraints seems to be driven by acto-myosin-based friction forces in agreement with Tambe et al. (17).

Conclusion

Our experimental approach, which offers control of many relevant system parameters, complemented by numerical simulations, allows exploring the role of boundary conditions on the collective behavior of migrating epithelial cells. We present direct evidence demonstrating that the geometrical constraints induce the emergence of various modes of collective migration with internal dynamics that can span length scales larger than their constituents. A switch in the collective behavior of cells can be observed from the migration into wide channels that exhibit swirling motions with vortices of around approximately 100 μm as opposed to a directed contraction-relaxation-based type of migration into narrow channels. We also observed a decrease in the average velocity of the cell front while increasing the width of the strip. This result can be partly explained by the higher oriented organization of the cell sheets in the narrow channels as shown by

the order parameter (Fig. 3*G*) and the restricted migration along the length of the channels. In the same line, both theoretical (26) and experimental (38) studies suggest that geometrical confinements could reduce the instabilities of the cell front described as finger-like structures and thus promote the higher observed velocities. However, the large velocity fields and traction forces observed far away from the leading cell front in the narrow channels suggest that the local coordination also originates from the interactions with the boundaries of the strips rather than with the leading edge only. The correlation length displays a dependence on the channel width but only for those which are smaller than the correlation length attributed to the intrinsic dynamics of the epithelial cells (approximately 100 μm) similar to passive physical systems (34). However in our case, the dynamics of cell sheets is strongly driven by active processes which increase the complexity of the observed interactions. The dynamic behavior observed in our experiments could be determined by a multitude of physical and biological factors. Here we quantitatively demonstrated that the geometrical constraints as well as cell–cell interactions played a critical role in the collective migration of cells but other parameters such as cell density as well as the nature of the substrate can affect the long-range interactions in migrating MDCK cells (30, 32).

The systems behavior, as the width of the strip is varied, is reminiscent of phase transition observed in various systems from a relatively disordered regime to a more orderly behavior in response to changes in local density of the constituent particles (39–41). The numerical results have in particular confirmed that such a physical approach could account for the evolution of the order parameter as the width is varied. Altogether, our results show that geometrical constraints lead to the emergence of a more directed and ordered migration when the population is confined below its natural correlation length, which in turn is controlled by cell–cell interactions. Such modes of migration could indeed be altered by changes in the dynamics of mechanical interactions mediated by intercellular adhesion because isolated MDCK cells, MDCK cells treated with blebbistatin, as well as α-catenin knockdown cells exhibit highly altered collective dynamics. Because tissue migration comes in many shapes and sizes (25) and our results shed a unique perspective on how collective cell migration should be reinterpreted depending on its guidance by extrinsic cues.

Materials and Methods

The fibronectin pattern studied here consists of a large rectangle (reservoir) joined to strips of varying widths (approximately 400 to 20 μm, Fig. 1). Microcontact printing was performed using PDMS stamps inked with a mixture of fibronectin and Cy3-conjugated fibronectin (27). A block of PDMS was placed on the pattern to cover the strips leaving the reservoir open for seeding cells. Particle image velocimetry (PIV) and micropillar arrays were used for analyzing velocity fields and traction forces, respectively. (See *SI Materials and Methods* for a detailed description).

ACKNOWLEDGMENTS. The authors thank N. Borghi, M.-A. Fardin, P. Matsudaira, J.-M. di Meglio, W.J. Nelson, M.P. Sheetz, M. Thery, Y. Toyama, V. Viasnoff, and R. Zaidel-Bar; the laboratory members of the Mechanobiology Institute for fruitful discussions and W.J. Nelson (Stanford University) for providing α-catenin knockdown cells. Financial supports from the Association pour la Recherche sur le Cancer (ARC), the Association Française contre la Myopathie (AFM), the Agence Nationale de la Recherche (ANR 2010 BLAN 1515 ; to B.L), the Human Frontier Science Program (Grant RGP0040/2012), and the Mechanobiology Institute (Team project funding) are gratefully acknowledged. The research was conducted in the scope of the International Associated Laboratory Cell Adhesion France Singapore (CAFS).

1. Forterre Y, Pouliquen O (2008) Flows of dense granular media. *Annu Rev Fluid Mech* 40:1–24.
2. Nagy M, Akos Z, Biro D, Vicsek T (2010) Hierarchical group dynamics in pigeon flocks. *Nature* 464:890–893.
3. Budrene EO, Berg HC (1995) Dynamics of formation of symmetrical patterns by chemotactic bacteria. *Nature* 376:49–53.
4. Ingber DE (2006) Mechanical control of tissue morphogenesis during embryological development. *Int J Dev Biol* 50:255–266.
5. Weijer CJ (2009) Collective cell migration in development. *J Cell Sci* 122:3215–3223.
6. Keller R (2002) Shaping the vertebrate body plan by polarized embryonic cell movements. *Science* 298:1950–1954.
7. Farooqui R, Fenteany G (2005) Multiple rows of cells behind an epithelial wound edge extend cryptic lamellipodia to collectively drive cell-sheet movement. *J Cell Sci* 118:51–63.
8. Friedl P, et al. (1995) Migration of coordinated cell clusters in mesenchymal and epithelial cancer explants in vitro. *Cancer Res* 55:4557–4560.
9. Tsuji T, Ibaragi S, Hu GF (2009) Epithelial-mesenchymal transition and cell cooperativity in metastasis. *Cancer Res* 69:7135–7139.
10. Borghi N, Lowndes M, Maruthamuthu V, Gardel ML, Nelson WJ (2010) Regulation of cell motile behavior by crosstalk between cadherin- and integrin-mediated adhesions. *Proc Natl Acad Sci USA* 107:13324–13329.
11. Keren K, et al. (2008) Mechanism of shape determination in motile cells. *Nature* 453:475–480.
12. Giannone G, et al. (2004) Periodic lamellipodial contractions correlate with rearward actin waves. *Cell* 116:431–443.
13. Trepat X, et al. (2009) Physical forces during collective cell migration. *Nat Phys* 5:426–430.
14. Gov NS (2009) Traction forces during collective cell motion. *HFSP J* 3:223–227.
15. Kim JH, Dooling LJ, Asthagiri AR (2010) Intercellular mechanotransduction during multicellular morphodynamics. *J R Soc Interface* 7:S341–S350.
16. Saez A, et al. (2010) Traction forces exerted by epithelial cell sheets. *J Phys Condens Matter* 22:194119.
17. Tambe DT, et al. (2011) Collective cell guidance by cooperative intercellular forces. *Nat Mater* 10:469–475.
18. Khalil AA, Friedl P (2010) Determinants of leader cells in collective cell migration. *Integr Biol* 2:568–574.
19. Lecaudey V, Cakan-Akdogan G, Norton WH, Gilmour D (2008) Dynamic Fgf signaling couples morphogenesis and migration in the zebrafish lateral line primordium. *Development* 135:2695–2705.
20. Doyle AD, Wang FW, Matsumoto K, Yamada KM (2009) One-dimensional topography underlies three-dimensional fibrillar cell migration. *J Cell Biol* 184:481–490.
21. Poujade M, et al. (2007) Collective migration of an epithelial monolayer in response to a model wound. *Proc Natl Acad Sci USA* 104:15988–15993.
22. Petitjean L, et al. (2010) Velocity fields in a collectively migrating epithelium. *Biophys J* 98:1790–1800.
23. Ilina O, Bakker GJ, Vasaturo A, Hofmann RM, Friedl P (2011) Two-photon laser-generated microtracks in 3D collagen lattices: Principles of MMP-dependent and -independent collective cancer cell invasion. *Phys Biol* 8:015010.
24. Andrew DJ, Ewald AJ (2010) Morphogenesis of epithelial tubes: Insights into tube formation, elongation, and elaboration. *Dev Biol* 341:34–55.
25. Friedl P, Gilmour D (2009) Collective cell migration in morphogenesis, regeneration and cancer. *Nat Rev Mol Cell Biol* 10:445–457.
26. Mark S, et al. (2010) Physical model of the dynamic instability in an expanding cell culture. *Biophys J* 98:361–370.
27. Fink J, et al. (2007) Comparative study and improvement of current cell micropatterning techniques. *Lab Chip* 7:672–680.
28. du Roure O, et al. (2005) Force mapping in epithelial cell migration. *Proc Natl Acad Sci USA* 102:2390–2395.
29. Nikolic DL, Boettiger AN, Bar-Sagi D, Carbeck JD, Shvartsman SY (2006) Role of boundary conditions in an experimental model of epithelial wound healing. *Am J Physiol Cell Physiol* 291:C68–C75.
30. Angelini TE, Hannezo E, Trepat X, Fredberg JJ, Weitz DA (2010) Cell migration driven by cooperative substrate deformation patterns. *Phys Rev Lett* 104:168104.
31. Angelini TE, et al. (2011) Glass-like dynamics of collective cell migration. *Proc Natl Acad Sci USA* 108:4714–4719.
32. Haga H, Irahara C, Kobayashi R, Nakagaki T, Kawabata K (2005) Collective movement of epithelial cells on a collagen gel substrate. *Biophys J* 88:2250–2256.
33. Lee P, Wolgemuth C (2011) Advent of complex flows in epithelial tissues. *Phys Rev E Stat Nonlin Soft Matter Phys* 83:061920.
34. Segrè PN, Herbolzheimer E, Chaikin PM (1997) Long-range correlations in sedimentation. *Phys Rev Lett* 79:2574–2577.
35. Kabla AJ (2011) *Collective Cell Migration: Leadership, Invasion and Segregation*, Available at http://arxiv.org/abs/1108.4286v1 [q-bio.CB].
36. Benjamin JM, et al. (2010) AlphaE-catenin regulates actin dynamics independently of cadherin-mediated cell-cell adhesion. *J Cell Biol* 189:339–352.
37. Vitorino P, Hammer M, Kim J, Meyer T (2011) A steering model of endothelial sheet migration recapitulates monolayer integrity and directed collective migration. *Mol Cell Biol* 31:342–350.
38. Lim JI, Sabouri-Ghomi M, Machacek M, Waterman CM, Danuser G (2010) Protrusion and actin assembly are coupled to the organization of lamellar contractile structures. *Exp Cell Res* 316:2027–2041.
39. Szabo B, et al. (2006) Phase transition in the collective migration of tissue cells: Experiment and model. *Phys Rev E Stat Nonlin Soft Matter Phys* 74:061908.
40. Schaller V, Weber C, Semmrich C, Frey E, Bausch AR (2010) Polar patterns of driven filaments. *Nature* 467:73–77.
41. Chaté H, Ginelli F, Grégoire G, Raynaud F (2008) Collective motion of self-propelled particles interacting without cohesion. *Phys Rev E* 77:046113.

Supporting Information

Vedula et al. 10.1073/pnas.1119313109

SI Text

SI Materials and Methods. ***Stamp preparation, cell seeding, and microscopy.*** Polydimethylsiloxane (PDMS) stamps for microcontact printing were prepared as described before (1). Molds of the pattern were first prepared using standard lithography methods. PDMS (Sylgard 184; Dow Corning) was prepared by mixing the base and curing agent in a ratio of 1 : 10 (wt/wt) and degassed. It was poured over the mold, degassed, and cured at 80 °C for 1 h. Stamps were peeled off the molds and plasma cleaned to make their surface hydrophilic. A mixture of Cy3 conjugated fibronectin and normal fibronectin (50 μg/mL; Sigma) was added immediately over the stamps to cover the whole surface. The mixture was allowed to be adsorbed for 45 min after which the excess fibronectin was removed with a pipette. The stamps were left in the laminar hood for approximately 10 min to dry. They were then gently pressed against the bottom of a non-culture-treated petri dish (Greiner) for about 1 min. The stamps were then carefully lifted up and the petri dishes were thoroughly rinsed with PBS. The patterns were visualized under a fluorescence microscope (Nikon). Petri dishes in which the fibronectin patterns were transferred properly were treated with a solution of 0.2% Pluronic F127 (Sigma) for 1 h to prevent cells from attaching and growing on the unstamped areas. After the incubation, the dishes were thoroughly rinsed several times with PBS to remove excess Pluronic F127.

Madin-Darby canine kidney (MDCK) cells were maintained in DMEM (Sigma) supplemented with 10% FBS (Hyclone) and 1% penicillin and streptomycin. Cells were seeded close to the edge of the PDMS block placed on the pattern and incubated overnight. The medium was removed the next day to wash off the unattached cells following which the PDMS block was lifted off. The petri dish was rinsed again with PBS to remove floating cells. Finally, culture medium was added and the petri dish was mounted on a microscope equipped with temperature, humidity, and CO_2 control (Olympus IX81) for live imaging. For some of the experiments, image acquisition was performed on Biostation (Nikon). Phase contrast images were acquired every 4 min using a 10 × objective. Acquisitions were typically obtained over a period varying from 12 to 24 h. For inhibiting myosin II, blebbistatin (stock 100 mM in DMSO; Tocris) was added at a final concentration of 50 μM after removing the PDMS block. Because the Biostation uses red light for illuminating the sample, there was no observable phototoxicity of blebbistatin.

Preparation of micropillars for traction force microscopy. Molds of silicon wafers containing the patterns (prepared using reactive ion etching) were first silanized. PDMS was poured onto the molds and allowed to cure at 120 °C for 15 min. The elastic modulus of PDMS cured under these conditions was found to be approximately 290 kPa, which translated into a spring constant of 10 nN/μm for the micropillars. The PDMS micropillars were gently peeled off in absolute alcohol and dried using a critical point dryer (Toussimis, Autosamdri-815) to prevent their collapse. Flat blocks of PDMS were incubated with a mixture of fluorescent and normal fibronectin (50 μg/mL) for 1 h. The solution was drained off and the stamps were dried thoroughly. The pillars were exposed to ultraviolet light in a UV cleaner (Nanoscience) for 30 min and stamped using the PDMS blocks prepared above. Stamping was confirmed using fluorescence microscopy. The pillars were then incubated in a 0.2% solution of Pluronic F127 (Sigma) for 30 min and then washed thoroughly with PBS. As described in the earlier section, a PDMS block was placed on the pillars such that it left the reservoir open for seeding cells. After cells reached confluence in the reservoir, the PDMS block was lifted to allow for cells to migrate into the channels containing arrays of micropillars. Fluorescent images of the top of the pillars were collected every 15 min for approximately 16 h on an upright microscope (Zeiss) equipped with an incubation system using a 63 × water immersion objective and coupled to an electron multiplying charge coupled device camera.

Image analysis. Particle image velocimetry (PIV) was performed using MatPIV package and implemented in MATLAB (2). Background subtractions of the input images were first performed in Image J to remove noise. Single cells ($n > 10$) were tracked using the manual tracking plugin for Image J and the result was used as input to determine the size of interrogation window for PIV as well as to confirm the accuracy of PIV. The correlation coefficients and curl of the velocity fields were also calculated in MATLAB. For traction force microscopy, images were first preprocessed in Image J to enhance contrast and subtract background. Drifts in the images were removed using an image stabilizing plugin [Image stabilizer plugin for ImageJ (3)]. Micropillars were 2 μm in diameter, 4 μm in height with a center to center spacing between the pillars of 4 μm. Pillar deflections were computed from the fluorescent images using a slightly modified custom code described previously (4). The noise level in the force measurement was estimated to be approximately 0.4 nN by averaging the forces registered in regions not covered by cells.

Staining and fluorescence microscopy. Cells were grown on patterned PDMS stamps coated with fibronectin. Cells were fixed for 15 min in 4% paraformaldehyde and permeabilized for 10 min using 0.1% Triton X-100 in PBS. For visualizing actin network, the fixed and permeabilized cells were incubated with Alexa488-labeled phalloidin for 30 min. To stain for E-cadherin, cells were fixed and permeabilized in ice cold methanol for approximately 3–5 min, blocked in a solution of 3% BSA in 0.1% Triton X-100 for 1 h, incubated with mouse primary antibody against E-cadherin (1 : 50 in blocking solution) for 1 h and finally incubated with Alexa488-conjugated goat anti-mouse antibody. Cells were washed with PBS and then mounted using Fluorsave (Calbiochem). Images were acquired on a confocal microscope (Leica SP5).

Calculation of the elongation factor, orientation index, order parameter, correlation coefficients, velocity fluctuations, and curl of velocity fields. Elongation factor and orientation index were computed by considering individual cells ($n > 30$) as ellipses. Elongation factor is the ratio of the major and minor axis and the orientation of the cell is considered to be the cosine of the angle between the major axis of the cell and the length of the fibronectin strip. The order parameter was defined as the cosine of the angle that the velocity vector makes with the length of the fibronectin strip. The order parameter varies from +1 (for velocity vectors parallel to the strip and directed along the direction of migration of the cell sheet) to −1 (for vectors that are directed opposite to the direction of migration of the cell front) through 0 (for those vectors that are directed perpendicular to the length of the strip).

The correlation coefficients were calculated using the following formulas:

$$C_u(\vec{r}) = \left\langle \frac{\langle u^*(\vec{r}' + \vec{r}, t) \times u^*(\vec{r}', t)\rangle \vec{r}}{[\langle u^*(\vec{r} + \vec{r}, t)^2\rangle \langle u^*(\vec{r}', t)^2\rangle]^{1/2}} \right\rangle t$$

$$C_v(\vec{r}) = \left\langle \frac{\langle v^*(\vec{r} + \vec{r}, t) \times v^*(\vec{r}', t)\rangle \vec{r}}{[\langle v^*(\vec{r} + \vec{r}, t)^2\rangle \langle v^*(\vec{r}', t)^2\rangle]^{1/2}} \right\rangle t$$

where C_u and C_v refer to the correlation coefficients in the directions perpendicular and parallel to the long axis of the fibronectin strip, respectively, u^* and v^* refer to the deviation of the velocity from the mean velocity in the directions perpendicular and parallel to the strip, $\vec{r}$ is the vector of the coordinates, and t refers to time. The spatial velocity correlation functions were evaluated by averaging the correlation coefficient over all the directions such that C_u and C_v are now functions of $\|\vec{r}\|$ (the norm of $\vec{r}$). The correlation length is the distance ($\|\vec{r}\|$) where the spatial velocity correlation function become zero. Velocity fluctuations perpendicular to the strip (ΔU) were computed by subtracting the average of the perpendicular component of all the velocity vectors and normalized by the average velocity of the migrating cell front (V_{mean}). The curl of the velocity fields gives an estimate of the rotation of the vectors over time. The curl function is defined as follows:

$$\nabla = \frac{\partial \mathrm{v}}{\partial \mathrm{x}} - \frac{\partial \mathrm{u}}{\partial \mathrm{y}}.$$

Actual computation was implemented using the in-built curl function in MATLAB.

Numerical simulation The numerical model is based on self-propelled cells interacting through adhesion and excluded volume interactions. The polarity of each cell, controlling the direction of its motile force, evolves as a result of a feedback from the cell displacement, with a certain persistence time. This framework, implemented using a cellular Potts model (5), proved to quantitatively reproduce correlations patterns in dense MDCK cell populations (6) . The particular code used here has been described and characterized in ref. 7. The main physical parameters of the model are the membrane energy, the cell motile force, and the persistence time of the cell polarity. These quantities account for cell stiffness, cell adhesion, and cell migration, and control the correlation length of the cell velocities in unconstrained conditions.

To test quantitatively if the simple mechanical interactions introduced in the model can explain the change in behavior between wide and narrow channels, simulations were run with parameters such that the unconstrained correlation length is comparable with the experimental value (about 10 cell diameters). The model was used to simulate dense populations of $N \times N$ cells confined in a biperiodic domain, for values of N ranging from 3 to 40 cells. The order parameter in the population was then calculated and plotted as a function of the population width N (Fig. S1*D*) to allow comparison with Fig. 3*G*.

1. Fink J, et al. (2007) Comparative study and improvement of current cell micro-patterning techniques. *Lab Chip* 7:672–680.
2. Sveen JK (2006) MatPIV—the PIV toolbox for MATLAB. Available at http://folk.uio.no/jks/matpiv/Download/.
3. K. Li (2008) The image stabilizer plugin for ImageJ. www.cs.cmu.edu/~kangli/code/Image_Stabilizer.html.
4. du Roure O, et al. (2005) Force mapping in epithelial cell migration. *Proc Natl Acad Sci USA* 102:2390–2395.
5. Graner F, Glazier JA (1992) Simulation of biological cell sorting using a two-dimensional extended Potts model. *Phys Rev Lett* 69:2013–2016.
6. Szabo A, et al. (2010) Collective cell motion in endothelial monolayers. *Phys Biol* 7:046007.
7. Kabla AJ (2011) *Collective Cell Migration: Leadership, Invasion and Segregation*. Available at http://arxiv.org/abs/1108.4286v1 [q-bio.CB].

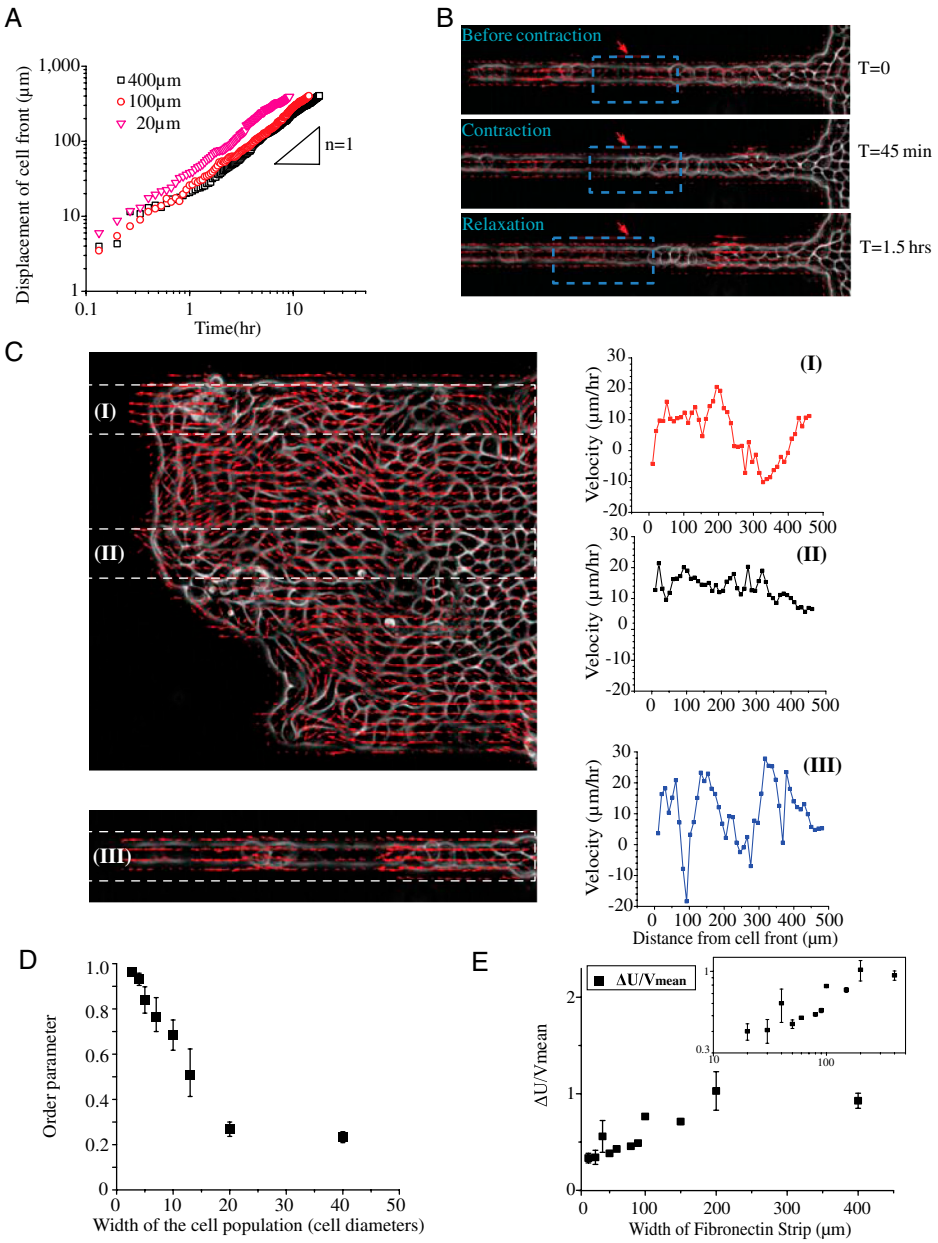

Fig. S1. (*A*) Displacement of the average cell front as a function of time in strips of different widths on a log–log scale. Progression of the cell front is nearly linear with slope (*n*) equal to unity. (*B*) Contraction-elongation cycle in 20-μm wide strips typically spans over three to six cells or approximately 100 μm. The mean period for contraction and relaxation of cell clusters is 1.5 h. Each cycle involves three to six cells, and it spans across approximately 100 μm. (*C*) Velocity profile along the edge (*Top*) and middle of the 400-μm wide strips (*Middle*) compared to the velocity profile along the 20-μm wide strips (*Bottom*). Higher magnitudes and fluctuations are observed in the 20-μm wide strips and on the edge of the 400-μm wide strip. (*D*) Order parameter as a function of the width of the population (represented in cell diameters) obtained from a numerical model of collective cell migration. Following the notations used in ref. 7, the model parameters used to generate this data are $J = 5$, $\mu = 0.125$, $\tau = 10$ Monte Carlo steps, and $T = 2.5$, with a cell volume of 400 pixels. Each value is an average over three independent realizations and over 7,500 Monte Carlo steps for each of them. (*E*) Fluctuations in the velocity perpendicular to the length of the strip (ΔU) normalized by the mean migration velocity of the cell sheet (V) as a function of width of the fibronectin strips. (*Inset*) Log–log plot of the normalized velocity correlations as a function of the width of the fibronectin strips.

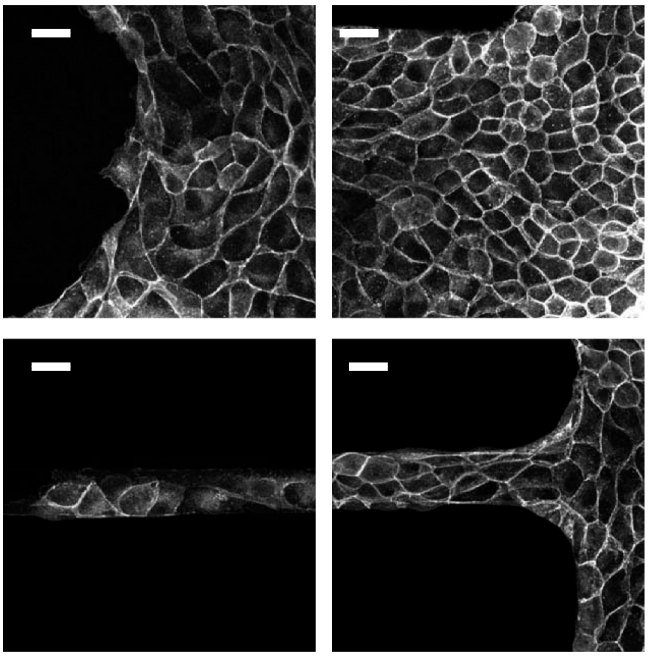

Fig. S2. Staining for E-cadherin at the leading front (*Left*) and far away from the leading front (*Right*) in MDCK cells migrating on 400-μm (*Top*) and 20-μm wide strips of fibronectin (*Bottom*). (Scale bars, 20 μm).

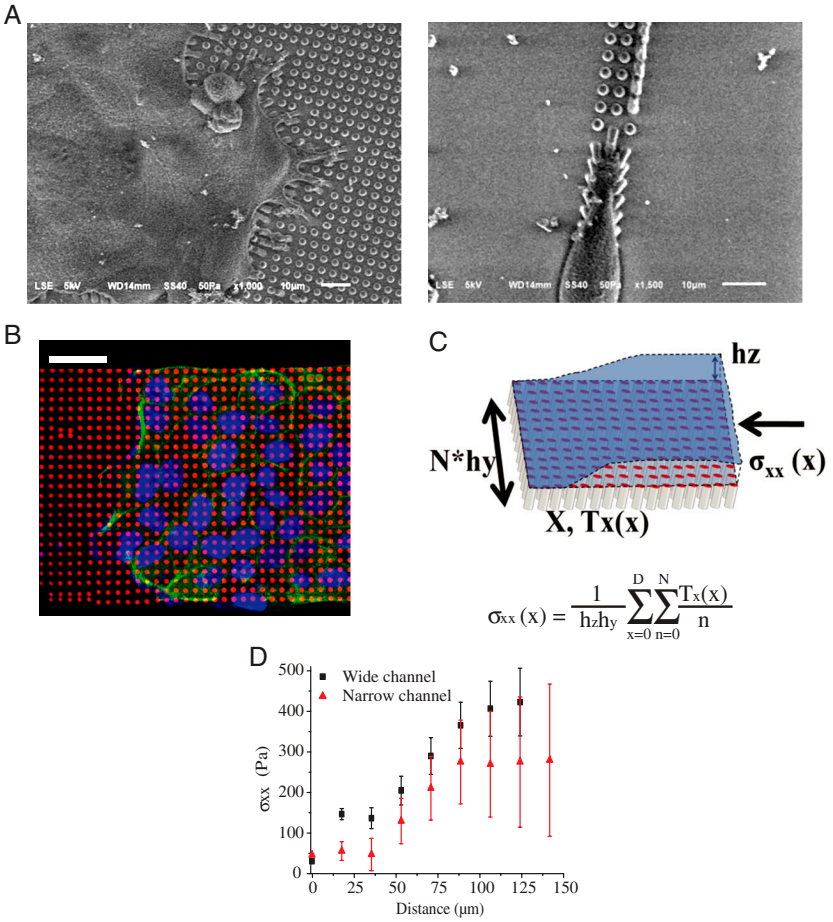

Fig. S3. (*A*) SEM images of MDCK cells migrating on wide (*Left*) and narrow (*Right*) strips of PDMS micropillars. (*B*) MDCK cells migrating on 100-μm wide strips of PDMS micropillars coated with fibronectin (red) and stained for actin (green). (*C*) Schematic diagram illustrating the stress $\sigma_{xx}(X)$ computation. Average stress $\sigma_{xx}(X)$ is computed by summation of the tractions with increasing distance (x) from the leading front. (*D*) Stress within the cell sheet increases with increasing distance for wider strips as observed by Trepat et al. (1). In the narrower strips, $\sigma_{xx}(X)$ reaches saturation approximately 100 μm away from the leading front. Alternative positive and negative forces arising from contraction-relaxation of cells can explain such a behavior (see text).

1 Trepat X, et al. (2009) Physical forces during collective cell migration. *Nat Phys* 5:426–430.

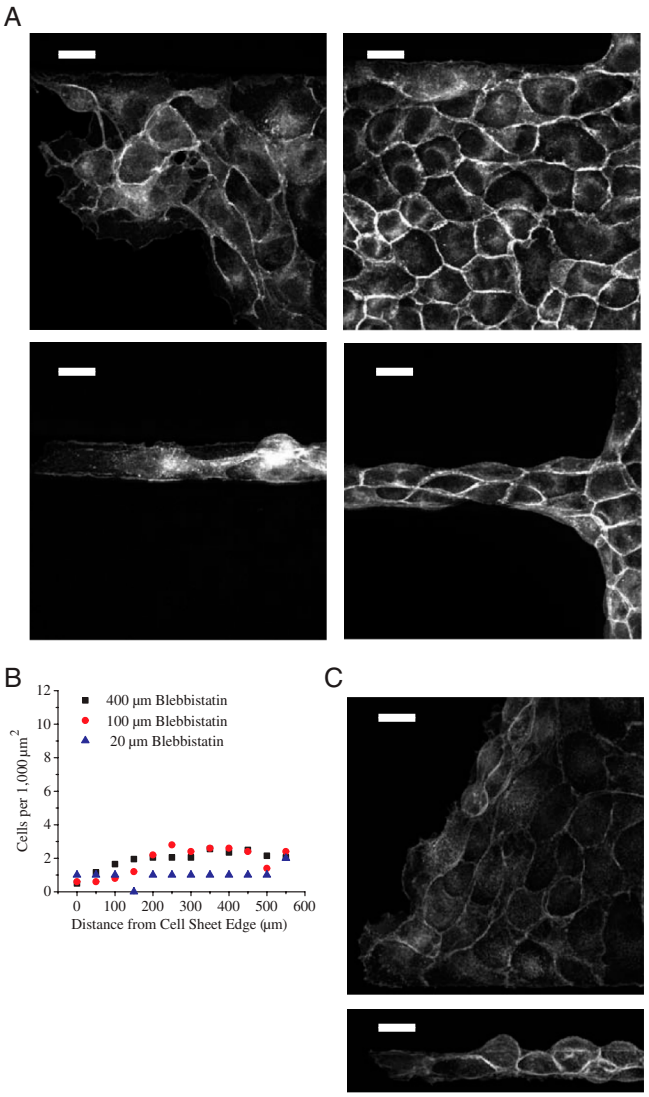

Fig. S4. (*A*) Staining for E-cadherin at the leading front (*Left*) and far away from the leading front (*Right*) in blebbistatin-treated MDCK cells migrating on 400-μm wide (*Top*) and 20-μm wide strips of fibronectin (*Bottom*). (Scale bar, 20 μm.) (*B*) Uniform cell density across strips of different widths and at different distance away from cell sheet edge. (*C*) Staining with phalloidin showing disrupted actin stress fibers in blebbistatin-treated MDCK cells.

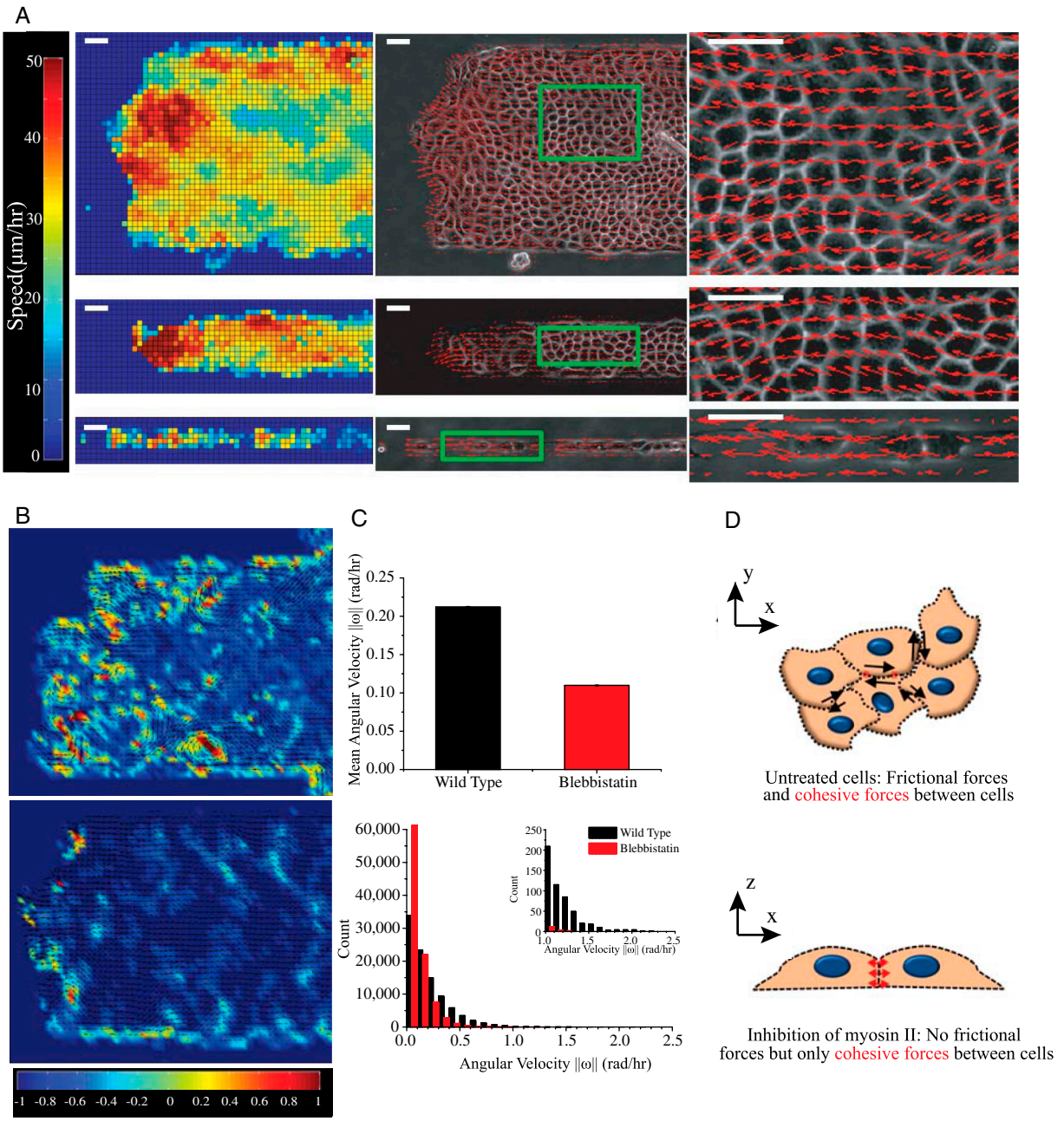

Fig. S5. Particle image velocimetry analysis of migrating epithelial sheets on wide, intermediate, and narrow strips of fibronectin after blebbistatin treatment. (*A*) Heat map showing typical spatial distribution of velocity fields at a given instant (*Left*) along 400-μm wide (*Top*), 100-μm wide (*Middle*), and 20-μm wide strips (*Bottom*). Blebbistatin-treated cells show less heterogeneity in velocity fields. Direction of velocity fields (*Middle*) show abrogation of vortex formation in 400-μm wide (*Top*), 100-μm wide (*Middle*), and 20-μm wide (*Bottom*) strips. Magnified views of region delimited by green boxes (*Right*). (Scale bars, 50 μm.) (*B*) Spatial distribution of angular velocity in the wide strips in the untreated (*Top*) and blebbistatin-treated (*Bottom*) cells. (*C*) Magnitude of the mean angular velocity decreases by 50% in cells treated with blebbistatin (*Top*). Frequency histogram of angular velocity profile shows a shift toward zero in the presence of blebbistatin (*Bottom*). *Inset* shows magnified distribution of the tail region of the histogram. (*D*) Cartoon depicting frictional forces (as viewed from the *Top*, *Left*) and cohesive forces (cross-sectional view, *Right*) between a pair of neighboring cells. Frictional forces induce reorganization and formation of vortices within the cell sheet. Addition of blebbistatin results in abrogation of the frictional forces, but not the cohesive forces resulting in a streamlined migration of the cell sheet without any vortex formation.

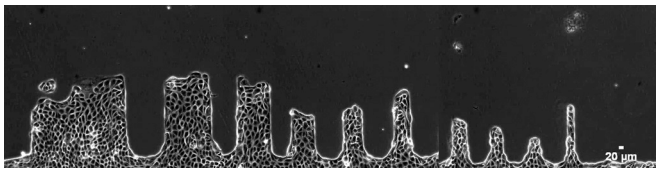

Movie S1. Migration of MDCK cells into fibronectin strips of different widths after the removal of a barrier. (Scale bar, 20 μm).
Movie S1 (MOV)

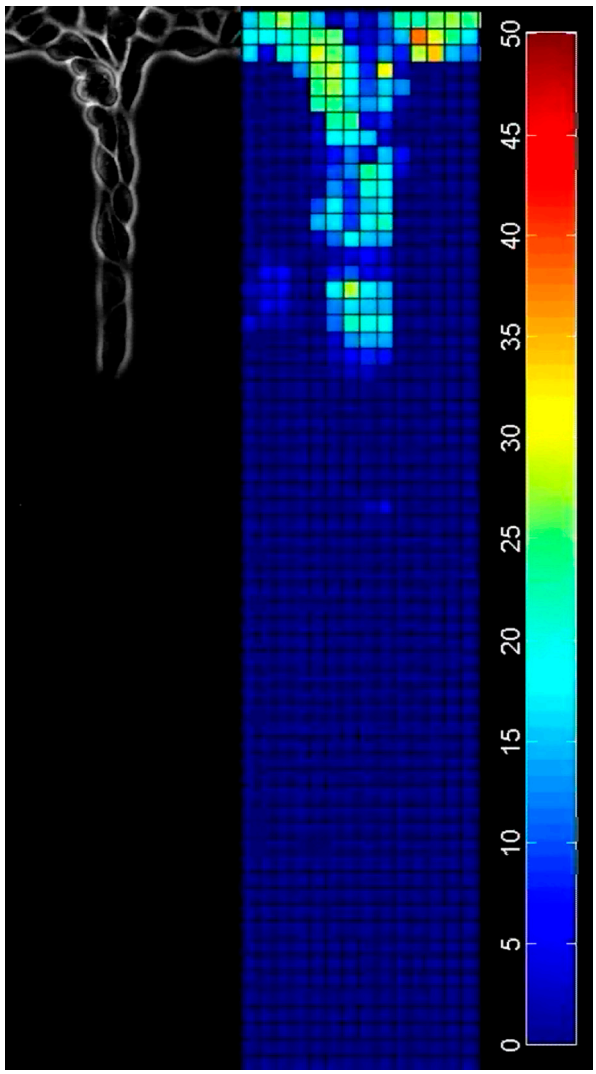

Movie S2. Caterpillar-like mode of migration in the 20-μm wide strip (*Left*) and magnitude of the velocity fields obtained using PIV (*Right*). Each frame is 20 min apart and video is played at 7 frames per second.

Movie S2 (MOV)

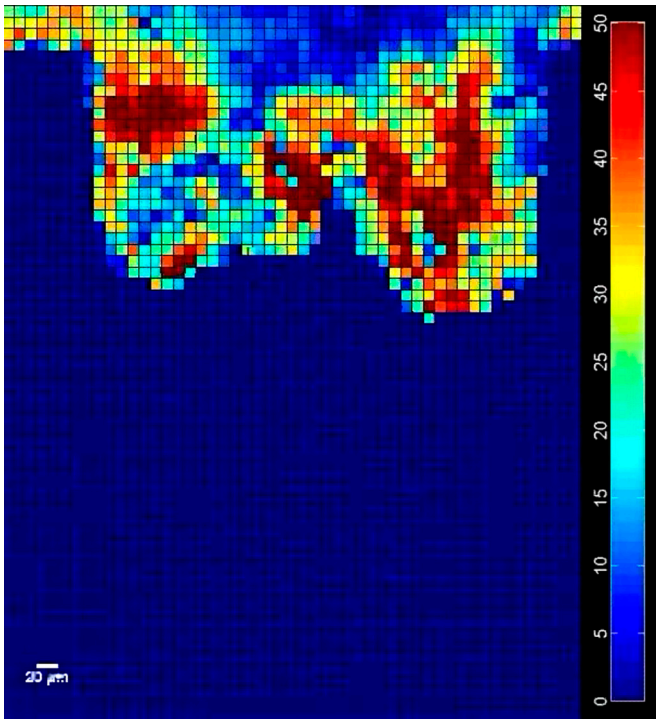

Movie S3. Magnitude of the velocity fields in MDCK cell sheets migrating on a 400-μm wide strip obtained using PIV. Each frame is 20 min apart and video is played at 7 frames per second.

Movie S3 (MOV)

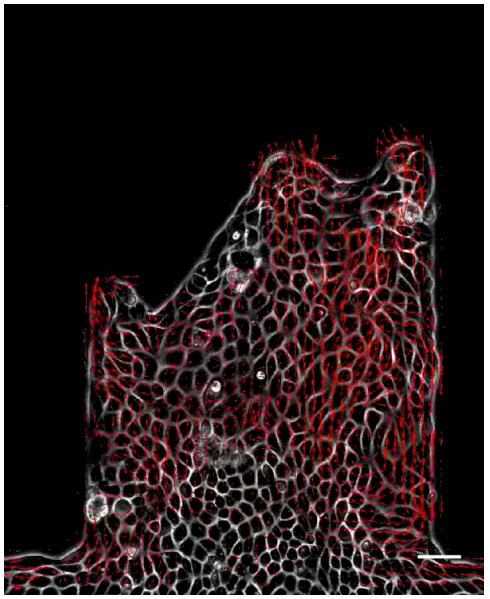

Movie S4. Direction of the velocity fields in MDCK cells sheets migrating on 400-μm wide strip showing transient vortex formation. Each frame is 20 min apart and video is played at 7 frames per second. (Scale bar, 50 μm.)

Movie S4 (MOV)

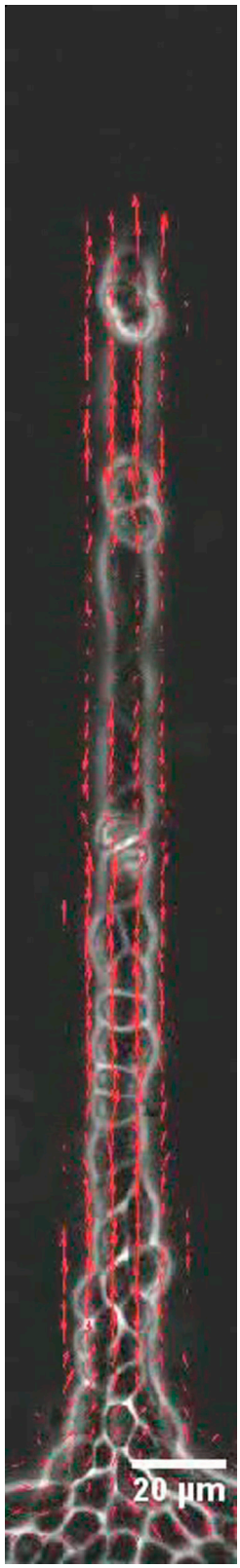

Movie S5. Direction of the velocity fields in MDCK cells sheets migrating on 20-μm wide strip showing caterpillar like migration and abrogation of vortices. Each frame is 20 min apart and video is played at 7 frames per second. (Scale bar, 20 μm).

Movie S5 (MOV)

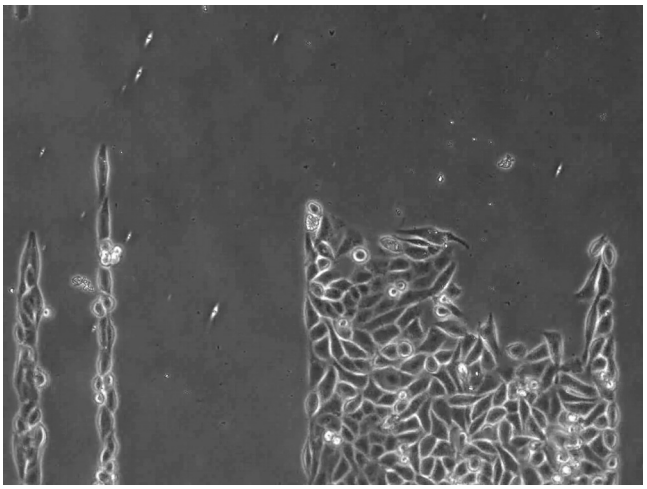

Movie S6. Migration of α-catenin knockdown MDCK cells on wide and narrow strips of fibronectin. Each frame is 4 min apart and video is played at 7 frames per second.

Movie S6 (MOV)

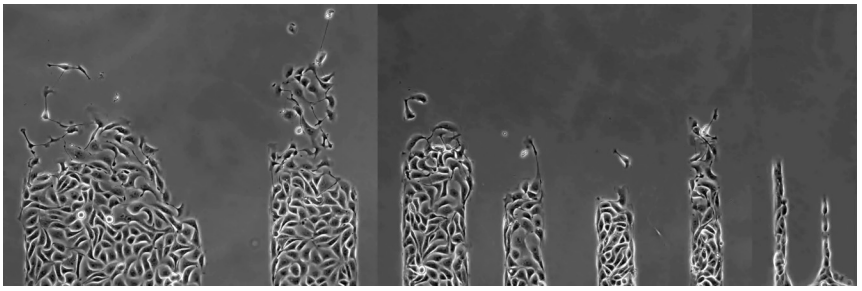

Movie S7. Migration of wild-type MDCK cells in low calcium medium. Each frame is 4 min apart and video is played at 7 frames per second.

Movie S7 (MOV)

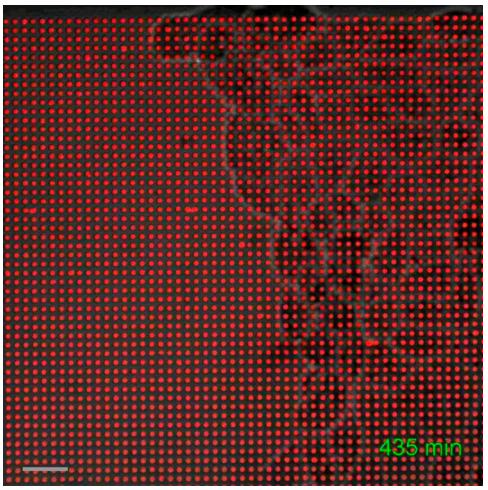

Movie S8. Migration of MDCK cells (phase image) overlayed on a fluorescent image of fibronectin-coated micropillars (2 μm diameter) on a 400-μm wide strip.

Movie S8 (MOV)

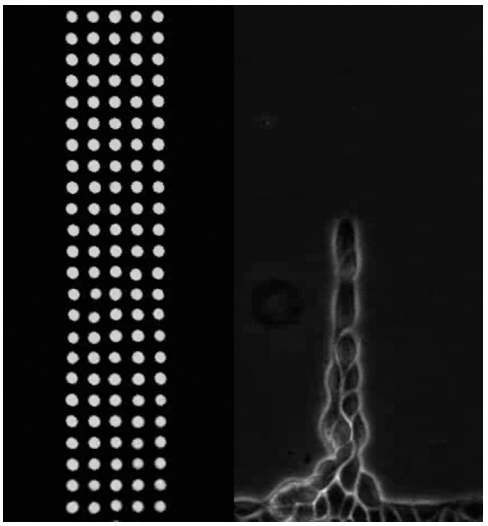

Movie S9. Deflection of pillars (2 μm diameter) in the narrow strips when cells migrate over them.
Movie S9 (MOV)

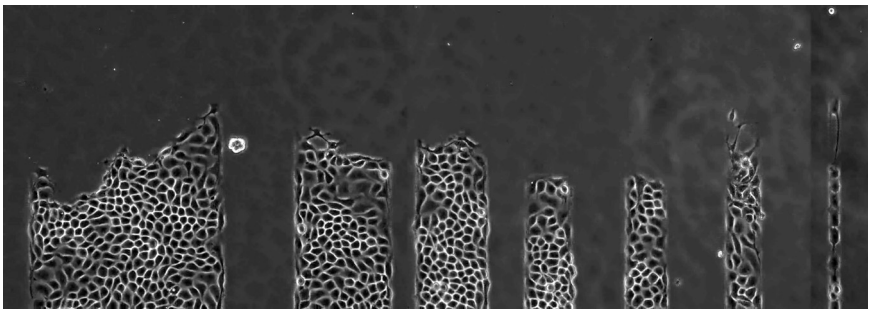

Movie S10. MDCK cells migrating on fibronectin strips of different widths in the presence of blebbistatin. Each frame is 4 min apart and video is played at 7 frames per second.

Movie S10 (MOV)